



A First-principle Model for Polarization Swings during Reconnection-powered Flares

David N. Hosking^{1,2} and Lorenzo Sironi³

¹ Oxford Astrophysics, Denys Wilkinson Building, Keble Road, Oxford OX1 3RH, UK; david.hosking@physics.ox.ac.uk

² Merton College, Merton Street, Oxford OX1 4JD, UK

³ Department of Astronomy and Columbia Astrophysics Laboratory, Columbia University, New York, NY 10027, USA; lsironi@astro.columbia.edu

Received 2020 July 29; accepted 2020 August 14; published 2020 September 4

Abstract

We show that magnetic reconnection in a magnetically dominated fast-cooling plasma can naturally produce bright flares accompanied by rotations in the synchrotron polarization vector. With particle-in-cell simulations of reconnection, we find that flares are powered by efficient particle acceleration at the interface of merging magnetic flux ropes, or “plasmoids.” The accelerated particles stream through the post-merger plasmoid toward the observer, thus progressively illuminating regions with varying plane-of-sky field direction, and so leading to a rotation in the observed polarization vector. Our results provide evidence for magnetic reconnection as the physical cause of high-energy flares from the relativistic jets of blazars (which recent observations have shown to be frequently associated with polarization rotations), and provide a first-principle physical mechanism for such flares.

Unified Astronomy Thesaurus concepts: [Blazars \(164\)](#); [Relativistic jets \(1390\)](#); [Polarimetry \(1278\)](#)

Supporting material: animation

1. Introduction

Magnetic reconnection in the relativistic regime (Lytikov & Uzdensky 2003; Lyubarsky 2005; Comisso & Asenjo 2014), where the magnetic energy density is even larger than the particle rest-mass energy density, has been invoked to explain the most dramatic flaring events in astrophysical high-energy sources, most notably the Crab Nebula gamma-ray flares (e.g., Cerutti et al. 2013; Yuan et al. 2016; Lyutikov et al. 2018) and GeV/TeV flares of blazars, a class of active galactic nuclei whose relativistic jet points toward Earth (e.g., Petropoulou et al. 2016; Ortuño-Macías & Nalewajko 2020; Mehlhaff et al. 2020).

Our understanding of the physics of relativistic reconnection has recently advanced thanks to fully kinetic particle-in-cell (PIC) simulations, which have established reconnection as a fast and efficient particle accelerator (e.g., Zenitani & Hoshino 2001; Guo et al. 2014; Sironi & Spitkovsky 2014; Werner et al. 2016). With regard to blazars, PIC simulations have demonstrated that reconnection can satisfy all the basic conditions for the emission: efficient dissipation, extended particle distributions, and rough equipartition between particles and magnetic field in the emitting region (Sironi et al. 2015; Petropoulou et al. 2019). In addition, the Doppler-boosted emission of fast “plasmoids” (or “flux ropes”) filled with high-energy particles and magnetic fields—an essential feature of reconnection (Loureiro et al. 2007; Uzdensky et al. 2010)—can power the ultrafast bright flares observed at GeV and TeV energies, whose duration can be even shorter than the light-travel time across the black hole that powers the jet (Petropoulou et al. 2016; Christie et al. 2019, 2020).

Large programs of polarimetric blazar monitoring (e.g., *RoboPol*; Angelakis et al. 2016) have recently provided valuable insights into the physics of blazar emission. In some cases, the electric vector position angle (PA) of the polarized emission displays long, smooth, and monotonic rotations (or “swings”) in the optical band, whose amplitudes are as high as hundreds of degrees (Marscher et al. 2008, 2010; Abdo et al. 2010; Larionov et al. 2013; Aleksić et al. 2014a, 2014b; Morozova et al. 2014; Chandra et al. 2015). These are generally associated with multiwavelength

flares and with a temporary decrease in optical polarization degree (PD; Blinov et al. 2015, 2016, 2018; Kiehlmann et al. 2016).

In this work, we argue that particle acceleration during plasmoid mergers naturally produces bright flares with associated synchrotron PA rotations, providing further evidence for magnetic reconnection as the physical process powering blazar flares. The PA rotations are caused by the apparent rotation of the plane-of-sky magnetic field when the merger-accelerated particles stream toward the observer through the post-merger plasmoid. We demonstrate this mechanism with PIC simulations of relativistic reconnection.

2. Numerical Setup

We employ 2.5D PIC simulations (i.e., 3D vector fields with translational invariance in z) performed with the TRISTAN-MP code (Buneman 1993; Spitkovsky 2005). The in-plane magnetic field is initialized in Harris sheet configuration, with the field along x and reversing at $y = 0$ (see Figure 1). We initiate reconnection by removing the thermal pressure of particles near the center of the sheet at the initial time, as in Sironi et al. (2016). The results we present in Section 4 are obtained at sufficiently late times for the system to have reached a statistically steady state, with no memory of the sheet initialization.

We parameterize the field strength B_0 by the magnetization, $\sigma \equiv B_0^2 / 4\pi n_0 m_e c^2 = (\omega_c / \omega_p)^2$, where $\omega_c = eB_0 / m_e c$ and $\omega_p = \sqrt{4\pi n_0 e^2 / m_e}$ are respectively the Larmor frequency and the plasma frequency for the cold electron–positron plasma outside the layer, with density n_0 . The Alfvén speed is related to the magnetization as $v_A / c = \sqrt{\sigma / (\sigma + 1)}$; we take $\sigma = 10$ so that $v_A \sim c$, as appropriate for blazar jets. In addition to the reversing in-plane field, we initialize a uniform “guide field” along $-\hat{z}$ with strength $B_g = 0.25 B_0$, which helps to provide pressure support to the cores of strongly cooled plasmoids; we comment on the effect of different guide-field strengths on polarization rotations in Section 5. We resolve the plasma skin depth c / ω_p with five cells, and initialize 16 particles in each cell. The numerical speed of light is 0.45 cells/time step. The box half-length in the x -direction is $L \simeq 4000$ cells = $800 c / \omega_p$. We employ outflow boundary conditions in x , while

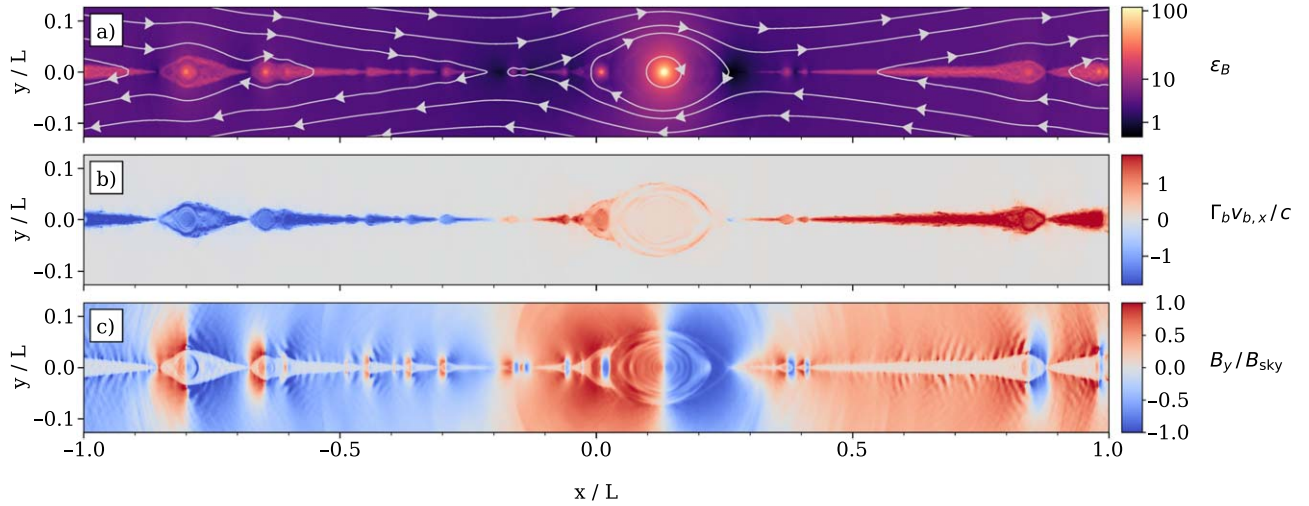


Figure 1. (a) Magnetic energy density normalized by the initial plasma rest-mass energy density, $\epsilon_B = B^2/8\pi n_0 m_e c^2$, with field lines in the xy -plane overlaid; magnetic tension drives fast outflows along the reconnection layer. (b) Bulk 4-velocity (in units of c), computed by averaging over particle velocities. Since large plasmoids tend to move slower than small ones due to their greater inertia, mergers between a small trailing plasmoid and a large leading plasmoid are common, e.g., at $x \simeq 0$. (c) B_y/B_{sky} , where $B_{\text{sky}} = (B_y^2 + B_z^2)^{1/2}$ is the strength of the plane-of-sky field for an observer at $x = \pm\infty$. Since the direction of \mathbf{B}_{sky} rotates within plasmoids, high-energy particles streaming through them naturally induce a PA swing.

along y two injectors continuously introduce fresh plasma and magnetic flux into the domain (for details see Sironi et al. 2016; Sironi & Beloborodov 2020). As opposed to the commonly adopted double-periodic boundaries, this setup allows us to evolve the system to arbitrarily long times, so we can study the statistical steady state for several Alfvénic crossing times (see the snapshot at $ct/L \simeq 6.7$ in Figure 1).

We compute the synchrotron emission (see, e.g., Cerutti et al. 2016) received by an observer at $x = +\infty$ assuming that the radiation is beamed along the particle motion, and including only particles whose velocity falls within a solid angle $\Omega/4\pi = 0.03$ around $+\hat{x}$. The corresponding cone is wider than the emission cone of particles with Lorentz factor $\gtrsim \sigma$, which dominate the emission. The inclusion of time retardation would not alter our results other than to reduce the duration of the flare and associated PA swing, and we neglect it for simplicity.

3. Plasma Conditions

Within the blazar class, flat-spectrum radio quasars (FSRQs) generally exhibit the strongest variability and polarized variability (Angelakis et al. 2016). For such systems, a hierarchy exists among the timescales (from fast to slow) on which (i) particles are accelerated, (ii) particles cool, and (iii) the dynamical time. Equivalently, $\gamma_{\text{cr}} \gg \gamma_{\text{acc}} \gg \gamma_{\text{cool}}$, where we define the following characteristic electron Lorentz factors: γ_{cr} , the “synchrotron burnoff limit” (de Jager & Harding 1992), at which synchrotron losses would prohibit further acceleration by the reconnection electric field $E_{\text{rec}} = \eta_{\text{rec}} B_0$ ($\eta_{\text{rec}} \sim 0.1$; e.g., Sironi et al. 2016), i.e.,

$$eE_{\text{rec}} \sim \frac{4}{3} \sigma_T \gamma_{\text{cr}}^2 \frac{B_0^2}{8\pi}; \quad (1)$$

γ_{acc} , the typical Lorentz factor to which particles are energized, which we estimate by assuming efficient conversion of magnetic energy to particle kinetic energy by reconnection, so $\gamma_{\text{acc}} \sim \sigma$;⁴

and γ_{cool} , from which particles would cool in a dynamical time $t_{\text{dyn}} = 2L/c$. Using Equation (1), we have

$$\gamma_{\text{cool}} \sim \frac{\gamma_{\text{cr}}^2}{\alpha_B \eta_{\text{rec}} \sqrt{\sigma}} \frac{c/\omega_p}{2L}, \quad (2)$$

where the factor $\alpha_B \sim 3$ reflects the fact that the mean field in plasmoids, where particles spend most of their life, is larger than B_0 (Sironi et al. 2016).

Typically, in FSRQs $\gamma_{\text{acc}} \sim 10^2\text{--}10^3 \ll \gamma_{\text{cr}}$ and $\gamma_{\text{cool}} \sim 0.01\text{--}0.1 \gamma_{\text{acc}} \sim 10$ (see Figure 3 in Ghisellini et al. 2010; see also Celotti & Ghisellini 2008; Böttcher et al. 2013; Sobacchi & Lyubarsky 2020). In our simulations, we employ $\gamma_{\text{acc}} \sim \sigma = 10$, $\gamma_{\text{cr}} = 40 \gg \gamma_{\text{acc}}$ and a system size of $2L \sim 1600 c/\omega_p$, so $\gamma_{\text{cool}} \sim 1 \sim 0.1 \gamma_{\text{acc}}$ as in blazar jets. Therefore, although our runs have smaller γ_{cr} , γ_{acc} , and γ_{cool} than blazar jets, they do satisfy the required hierarchy of time and energy scales. With our parameters, particles accelerated by reconnection up to $\gamma_{\text{acc}} \sim \sigma$ cool on a timescale $\sim (\gamma_{\text{cool}}/\gamma_{\text{acc}}) t_{\text{dyn}} \sim 0.2 L/c$, which is of the same order as the light-crossing time of the largest plasmoids, with diameter $w \sim 0.2 L$ (Sironi et al. 2016). This is important for our model, since a large PA swing is produced only if the emitting particles do not appreciably cool while moving through the post-merger plasmoid.

Numerically, we implement synchrotron cooling according to the reduced Landau–Lifshitz model (see Vranic et al. 2016). We do not include inverse Compton losses, which may indeed be the most important cooling mechanism in the brightest FSRQs (e.g., Celotti & Ghisellini 2008; Böttcher et al. 2013). While the presence of strong cooling is required to allow the sporadic flares associated with plasmoid mergers to dominate the quiescent emission, we do not expect the physical nature of the cooling to impact the occurrence or properties of PA swings, and indeed we have obtained qualitatively similar results when including inverse Compton losses.

4. Results

Figure 2 shows the lightcurve of high-frequency synchrotron emission (defined by the shaded band in Figure 3) seen by an

⁴ This is appropriate for an electron–positron plasma. For an electron–ion plasma, the typical Lorentz factor of electrons energized by reconnection is $\gamma_{\text{acc},e} \sim \sigma_i m_i/m_e \equiv \sigma_e$, where the magnetization $\sigma_i \equiv B_0^2/4\pi n_0 m_i c^2$ is now normalized to the ion rest-mass energy density.

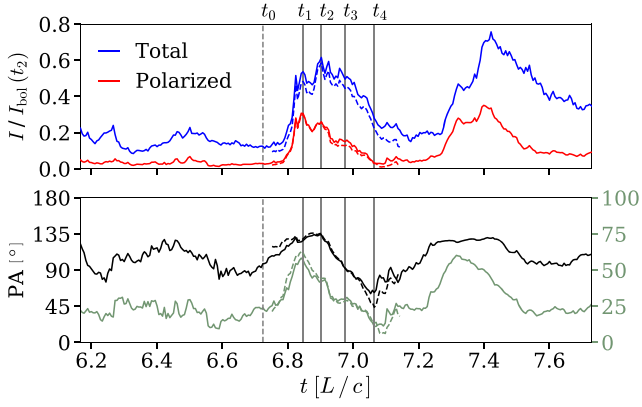


Figure 2. Top: lightcurves of total and polarized synchrotron intensity in the high-frequency band defined in Figure 3, for an observer at $x = +\infty$. Both are normalized to the peak bolometric flux at t_2 . Bottom: time series of the PA, measured counterclockwise from $+\hat{z}$, and the PD. Solid lines include the whole simulation domain, dashed lines only the region $0.04 L \leq x \leq 0.32 L$, which dominates the central flare.

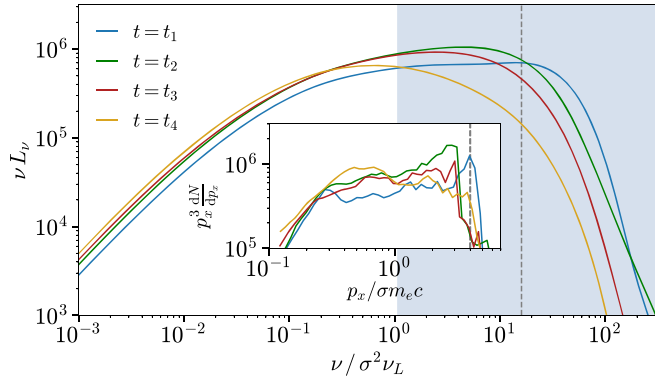


Figure 3. Synchrotron spectrum from the region $0.04 L \leq x \leq 0.32 L$ at the times t_i defined in the main text (see also Figure 2). The shaded area shows our chosen “high-frequency band.” The dashed vertical line is at $\nu = \gamma_{\text{cr}}^2 \nu_L$ (the so-called synchrotron burnoff frequency; de Jager & Harding 1992), where $\nu_L = \omega_c / (2\pi)$. Inset: distribution of x -momenta (in units of $\sigma m_e c$) for the particles contributing to the emission. The dashed line is at $p_x = \gamma_{\text{cr}} m_e c$.

observer at $x = +\infty$, together with the PA (measured counterclockwise from $+\hat{z}$) and the PD. The local polarization electric vector is orthogonal to the plane-of-sky (i.e., yz -plane) magnetic field (e.g., $\text{PA} = 90^\circ$ if the plane-of-sky field is along the z -direction of the guide field). In the prominent flare from $t \simeq 6.8 L/c$ to $t \simeq 7.1 L/c$ (the first flare in Figure 2), the synchrotron intensity increases by a factor of ~ 4 , while the PA rotates by $\simeq 70^\circ$. The flare is powered by particles accelerated as a small, fast “trailing” plasmoid (located at $-0.02 L < x < 0.03 L$ in Figure 1) merges into a larger and slower “leading” plasmoid (located at $0.03 L < x < 0.23 L$ in Figure 1). Most of the flare emission comes from this merger (compare solid and dashed lines in Figure 2). In addition to the pre-merger time t_0 displayed in Figure 1, we define the following times in Figure 2: t_1 , the peak of polarized flux and the maximum PD; t_2 , the peak of total flux and the maximum PA; t_3 , the midpoint of the polarization swing, when $\text{PA} = 90^\circ$; and t_4 , the minimum PA and PD.

Figure 4 presents the 2D bolometric synchrotron emissivity in the region of the merger, at each time t_i . The emission is dominated by merger-accelerated particles that stream around the post-merger plasmoid along its helical magnetic field,

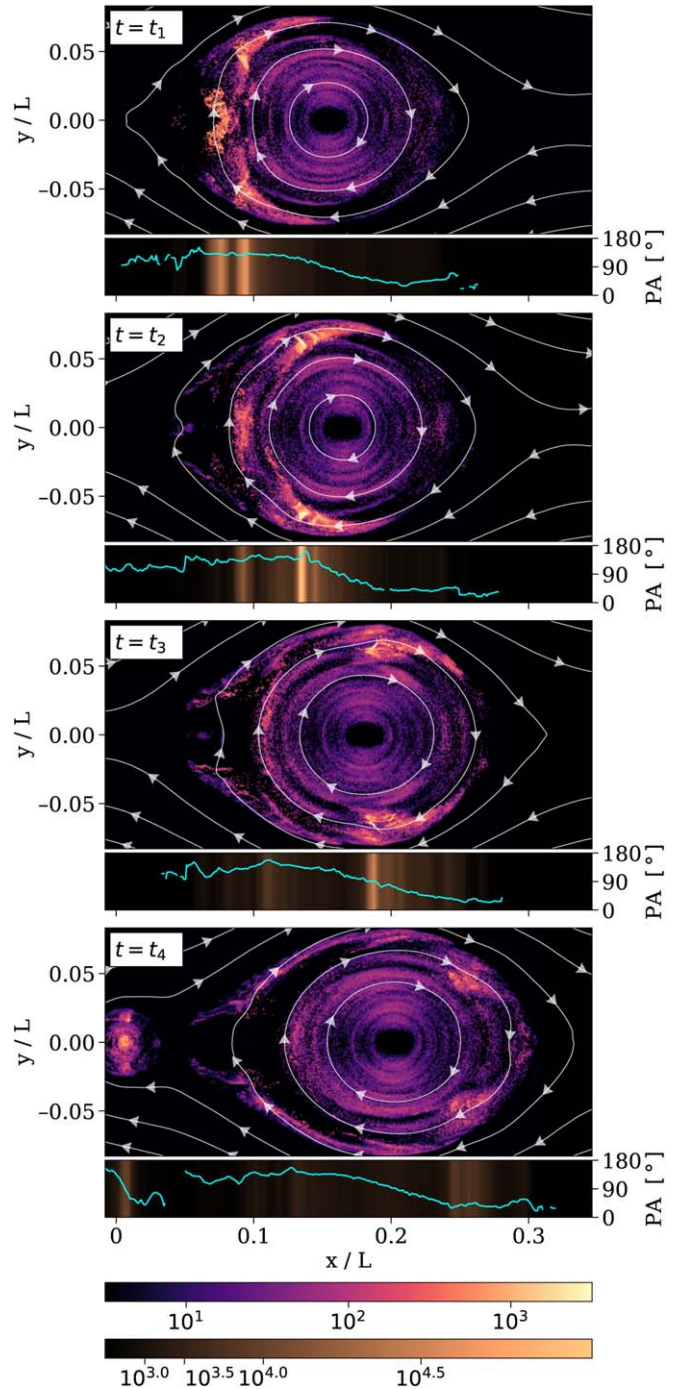


Figure 4. 2D bolometric synchrotron emissivity (upper color bar) received by an observer at $x = +\infty$ at the times t_i defined in the main text (see also Figure 2), with field lines in the xy -plane overlaid. Beneath each 2D plot, we show the y -integrated high-frequency luminosity (lower color bar) with PA overlaid in cyan. As the merger-accelerated particles stream through the plasmoid, they illuminate regions with varying plane-of-sky field, causing the PA swing.

(An animation of this figure is available.)

whose projection on the xy -plane is shown by the gray lines. As the accelerated particles move across the plasmoid, they create an “emission front” that sweeps through regions with varying plane-of-sky field direction (see also Figure 1(c)); in turn, this causes a rotation in the observed PA (see the bright band moving across the lower subpanels of Figure 4).

The flare emission rises on the merger timescale, which is approximately the light-crossing time of the small trailing plasmoid. The subsequent slower decay is due to cooling. A large PA swing requires the cooling time to be on the order of the light-crossing time of the larger, leading plasmoid, so that the emitting particles do not significantly cool before moving across the whole plasmoid. For particles at $\gamma_{\text{acc}} \sim \sigma$, the two timescales are indeed comparable, as previously discussed. The size disparity between the two merging plasmoids, and hence the fast rise compared to the slow decay, is essential as the accelerated particles must be localized within a small region in the post-merger plasmoid for their synchrotron emission to be strongly polarized. So, while the two merging plasmoids need to be sufficiently large to energize enough particles to power observable flares, detectable PA rotations only occur if their sizes are somewhat different.

We now describe the temporal evolution of the emission, using Figures 3 and 4. At t_1 , energetic particles accelerated by the merger are concentrated at the rear of the post-merger plasmoid. At this time (see Figure 3), the spectrum has a broad peak, dominated by particles with Lorentz factor $\gamma_{\text{pk}} \sim \text{few}\sigma$, and extends up to the synchrotron burnoff frequency $\nu = \gamma_{\text{cr}}^2 \nu_c$ (de Jager & Harding 1992), which for our simulation parameters ($\gamma_{\text{cr}} = 40$ and $\sigma = 10$) is only marginally greater. For true blazar conditions, where $\gamma_{\text{cr}} \gg \gamma_{\text{acc}} \sim \sigma$, we expect that the emission will extend up to the burnoff limit, but the spectral peak will be dominated by particles with $\gamma_{\text{pk}} \sim \text{few}\sigma$, given the steep spectral slopes typically produced by reconnection for blazar conditions (Ball et al. 2018; Petropoulou et al. 2019).

Subsequently, the energetic particles stream along the plasmoid field lines, and cool. By t_2 , Figure 3 shows that the peak frequency has dropped by a factor of ~ 3 due to cooling—however, the peak flux is greater, since ongoing acceleration has increased the number of energetic particles emitting toward the observer.

From t_2 to t_4 , the streaming of energetic particles around the plasmoid induces a PA rotation of $\simeq 70^\circ$, with the polarization vector rotating from $\simeq 135^\circ$ (measured counterclockwise from $+\hat{z}$), to $\simeq 65^\circ$. Meanwhile, cooling losses reduce both the peak frequency and the peak flux, since particle acceleration has ceased. The polarization degree decreases with time (its maximum is $\simeq 57\%$ at t_1) as the polarization signal is diluted by the spatial diffusion and cooling of high-energy particles. We note that a drop in optical PD during PA swings has been observed in blazars (Blinov et al. 2015). The peak PD and the amplitude of polarization swing are dependent on the chosen frequency band, both being larger when the band is restricted to higher frequencies, which are dominated by the most energetic particles. For example, if we focus only on frequencies higher than the peak frequency at t_2 , the maximum PD reaches $\simeq 72\%$,⁵ while the amplitude of the PA swing increases to $\simeq 90^\circ$.

By t_4 , the PA reaches its minimum, as most of the emitting particles have fully circled the plasmoid. By this time, strong cooling losses have reduced the synchrotron luminosity to pre-merger levels, and merger-accelerated particles no longer dominate the layer-integrated emission (see Figure 2).

We note that not all flares produced by plasmoid mergers are accompanied by large PA swings. For example, in the merger of two plasmoids of similar sizes, the emission is not

sufficiently localized to produce a strong rotation. Alternatively, when several small plasmoids merge with the tail of a large one over a timescale similar to the streaming time of accelerated particles, there is no appreciable PA swing because the emitting particles are distributed throughout the post-merger plasmoid (an example is the second flare in Figure 2, at $t \simeq 7.4 L/c$).

5. Discussion

Polarization swings associated with multiwavelength flares can help constrain the nature of high-energy emission from blazar jets. Existing theoretical models of blazar PA swings invoke geometric effects (Marscher et al. 2008, 2010; Lyutikov et al. 2017), stochastic processes in turbulent fields (Marscher 2014), or a local magnetic field alteration due to shocks or magnetic instabilities (Zhang et al. 2015, 2018; Nalewajko 2017; see the latter for a reconnection-based model). Our model belongs to the latter category. We have shown that particles accelerated during mergers of plasmoids produce both a bright flare and a simultaneous PA swing as they stream through the post-merger plasmoid while cooling.

To assess the expected emission frequency, let us assume that the typical Lorentz factor of jet electrons is $\sim 3 \times 10^2$, and that the magnetic field strength is $\mathcal{B} = 1 \mathcal{B}_0 \text{ G}$ (Celotti & Ghisellini 2008; Ghisellini et al. 2010; Böttcher et al. 2013). In reconnection, the mean magnetic energy per particle, $\sigma/2$, is equally divided between accelerated particles and reconnected magnetic fields, giving a mean Lorentz factor of $\sim \sigma/4$ (see Sironi et al. 2015). Therefore, we require $\sigma \sim 10^3$ (for an electron–ion plasma, this constraint corresponds to $\sigma_e \sim 10^3$, so the ion-normalized magnetization is $\sigma_i \sim 1$). The peak emission is from particles with $\gamma_{\text{pk}} \sim 3\sigma$ (see Figure 3), whose synchrotron emission frequency is

$$\nu_{\text{obs}} \simeq 5 \times 10^{14} \Gamma_{j,1} \left(\frac{\gamma_{\text{pk}}}{3 \times 10^3} \right)^2 \mathcal{B}_0 \text{ Hz}, \quad (3)$$

for a jet with Lorentz factor of $\Gamma_j = 10 \Gamma_{j,1}$, viewed from an angle of $1/\Gamma_j$ from the axis. So, the peak frequency is indeed expected to fall in the optical band.

We can estimate the timescale for flares according to our model as follows. In the rest frame of the jet, the time for a PA rotation is the time taken for accelerated particles to circle the post-merger plasmoid, which is

$$T_{\text{jet}} = \frac{w}{v_{\text{front}}} \sim \frac{0.2L}{c}, \quad (4)$$

where we have taken $w \sim 0.2 L$ as the characteristic width of the large post-merger plasmoid, which we assume to move at nonrelativistic speeds, and $v_{\text{front}} = \beta_{\text{front}} c \lesssim c$ is the speed at which the emission front of accelerated particles sweeps through the plasmoid. The resulting timescale matches our results in Figure 2 well (when including time retardation, the PA swing duration will be somewhat shorter). The length L of the layer can be computed by assuming a jet dissipation distance of $\sim 1 \text{ pc}$ from the black hole and a jet opening angle of $\sim 0.1 \text{ rad}$, so we expect current sheets of size $L = 3 \times 10^{17} L_{17.5} \text{ cm}$. The observed timescale will be

$$T_{\text{obs}} \sim \frac{1}{\Gamma_j} T_{\text{jet}} \simeq 2 \Gamma_{j,1}^{-1} L_{17.5} \beta_{\text{front}}^{-1} \text{ days}. \quad (5)$$

⁵ This is close to the theoretical maximum PD of 75%, corresponding to monoenergetic particles. Indeed, the inset of Figure 3 shows a sharp peak in the momentum spectrum at this time.

This is around the lower limit of rotation durations detectable by current polarization monitoring programs, owing to limited cadence of observations and the 180° ambiguity in the PA, but it is consistent as an order-of-magnitude estimate (see, e.g., Blinov et al. 2016). Within our model, we argue that many PA rotations may occur on a timescale that is too short to be detectable, while those that are detected are somewhat rarer events corresponding to particularly large plasmoids, or to the cumulative effect of several consecutive mergers (see below).

In our model, the cooling time of the optical-emitting particles needs to be somewhat shorter than the light-crossing time of large plasmoids. In fact, for particles at the peak Lorentz factor $\gamma_{\text{pk}} \sim 3\sigma$, the cooling time is $\sim 0.06 L/c \sim 0.3 T_{\text{jet}}$ (see Section 3 and Equation (4)). Given this, we expect that at higher frequencies (e.g., X-rays), the emitting particles will cool even faster, well before circling the post-merger plasmoid. It is therefore a prediction of our model that there should be no appreciable PA rotations in the X-ray band. At frequencies much below the optical band, the longer particle-cooling time implies that a larger fraction of the layer will simultaneously contribute to the emission, prohibiting significant PA rotations.

Our simulation parameters produce PA swings of $\sim 90^\circ$; this is consistent with rotations coincident with bright gamma-ray flares (Blinov et al. 2018).⁶ Even larger swings have been observed (e.g., Marscher et al. 2010; Chandra et al. 2015). With regard to this, we point out that in the limit $B_g/B_0 \ll 1$, our proposed mechanism naturally leads to PA swings of 180° , which is the most commonly observed rotation amplitude (Blinov et al. 2016). Indeed, within the reconnection scenario, configurations with weaker guide fields better satisfy the blazar constraints of high efficiency and rough equipartition between particles and fields (Sironi et al. 2015). Rotation amplitudes even larger than 180° can be accounted for in our model as a result of consecutive mergers of a chain of small, trailing plasmoids with a large, leading one. If $B_g/B_0 \ll 1$, the resulting series of flares and corresponding PA rotations could be cumulatively interpreted as a single flaring episode with continuous PA swing of more than 180° . Indeed, we note that the PA rotation of $\sim 720^\circ$ in PKS 1510–089 (Marscher et al. 2010) occurred over a 50 day period encompassing six gamma-ray flares.

We note that, for a given reconnection geometry and observer’s line of sight, our model generally predicts PA swings in one particular direction. While expected to be rarer, swings in the opposite direction (e.g., Chandra et al. 2015) can be produced in the same geometry by the merger of a *small* leading plasmoid with a *larger* trailing one. Particles accelerated at the merger interface stream backwards through the post-merger plasmoid, so our mechanism occurs in reverse, though with reduced intensity due to the smaller Doppler boosting. More commonly, swings in the opposite direction will be produced by a layer with opposite guide-field orientation. Thus, for a given object we do not generally expect a preference for PA rotations in any particular direction, which is consistent with observations.

We conclude with a few remarks and caveats. As compared to the pioneering work by Zhang et al. (2018), who also employed PIC simulations of relativistic reconnection to explain PA rotations in blazars, (i) we provide a physically grounded explanation for PA swings and their association with multi-wavelength flares and reduced optical PD (Blinov et al. 2015);

(ii) we emphasize that PA rotations naturally occur if the observer’s line of sight is along the reconnection outflow, which is also required to explain ultrafast GeV and TeV flares in blazars (Giannios 2013; Petropoulou et al. 2016; Christie et al. 2019, 2020); (iii) we self-consistently retain the anisotropy of emitting particles.

Our simulations have been initialized with the somewhat idealized Harris sheet reconnection geometry. We do not view this as a major limitation, as the merger discussed in Section 4 occurs ~ 7 layer-light-crossing times after the sheet is initialized, so we expect the state of the system at this time to be insensitive to choices at initialization. We acknowledge, however, that the global geometry of reconnection layers in the jet may be more complicated than the planar setup considered here. Understanding the statistics of polarization rotations resulting from different layer properties will require a further detailed study, though we speculate that polarimetric measurements may ultimately be useful to distinguish whether current sheets are introduced at the jet base (in so-called “striped jets”; e.g., Giannios & Uzdensky 2019) or whether they are produced by the nonlinear development of MHD instabilities, like the kink mode (e.g., Bodo et al. 2020).

Although we have presented results for a pair plasma, we expect that our model will also hold in relativistic electron–proton and electron–positron–proton reconnection, since leptons still pick up a significant fraction of the dissipated magnetic energy (Rowan et al. 2017, 2019; Werner et al. 2018; Petropoulou et al. 2019). We defer an investigation of the more complex 3D case to future work, though we note that mergers of plasmoids are observed in 3D simulations of relativistic reconnection (e.g., Guo et al. 2014; Sironi & Spitkovsky 2014; Werner & Uzdensky 2017; Sironi & Beloborodov 2020), so we expect our model to be applicable to the 3D case.

Finally, we reiterate that we have not included inverse Compton losses, which may indeed be the most important cooling mechanism in the brightest FSRQs. While we do not expect the physical nature of the cooling to impact the occurrence or properties of PA swings, a self-consistent inclusion of both inverse Compton and synchrotron cooling will be required for direct comparison to the multiwavelength polarimetric signatures of blazars.

We thank D. Blinov, L. Comisso, D. Giannios, E. Sobacchi, F. Tavecchio, and H. Zhang for useful feedback. This research was carried out in part during the 2019 Summer School at the Center for Computational Astrophysics, Flatiron Institute. The Flatiron Institute is supported by the Simons Foundation. D.N.H. is supported by a UK STFC studentship. L.S. acknowledges support from the Sloan Fellowship, the Cottrell Scholar Award, DoE DE-SC0016542, NSF ACI-1657507, NASA ATP NNX17AG21G, and NSF PHY-1903412. The simulations have been performed at Columbia (Habanero and Terremoto), and with NERSC (Cori) resources.

ORCID iDs

David N. Hosking  <https://orcid.org/0000-0002-7958-6993>
Lorenzo Sironi  <https://orcid.org/0000-0002-5951-0756>

References

- Abdo, A. A., Ackermann, M., Ajello, M., et al. 2010, *Natur*, 463, 919
Aleksić, J., Ansoldi, S., Antonelli, L. A., et al. 2014a, *A&A*, 567, A41
Aleksić, J., Ansoldi, S., Antonelli, L. A., et al. 2014b, *A&A*, 569, A46

⁶ Most observational campaigns only select PA swings $>90^\circ$.

- Angelakis, E., Hovatta, T., Blinov, D., et al. 2016, *MNRAS*, **463**, 3365
- Ball, D., Sironi, L., & Özel, F. 2018, *ApJ*, **862**, 80
- Blinov, D., Pavlidou, V., Papadakis, I., et al. 2015, *MNRAS*, **453**, 1669
- Blinov, D., Pavlidou, V., Papadakis, I., et al. 2018, *MNRAS*, **474**, 1296
- Blinov, D., Pavlidou, V., Papadakis, I. E., et al. 2016, *MNRAS*, **457**, 2252
- Bodo, G., Tavecchio, F., & Sironi, L. 2020, arXiv:2006.14976
- Böttcher, M., Reimer, A., Sweeney, K., & Prakash, A. 2013, *ApJ*, **768**, 54
- Buneman, O. 1993, *PhRv*, **80**, 692
- Celotti, A., & Ghisellini, G. 2008, *MNRAS*, **385**, 283
- Cerutti, B., Mortier, J., & Philippov, A. A. 2016, *MNRAS*, **463**, L89
- Cerutti, B., Werner, G. R., Uzdensky, D. A., & Begelman, M. C. 2013, *ApJ*, **770**, 147
- Chandra, S., Zhang, H., Kushwaha, P., et al. 2015, *ApJ*, **809**, 130
- Christie, I. M., Petropoulou, M., Sironi, L., & Giannios, D. 2019, *MNRAS*, **482**, 65
- Christie, I. M., Petropoulou, M., Sironi, L., & Giannios, D. 2020, *MNRAS*, **492**, 549
- Comisso, L., & Asenjo, F. A. 2014, *PhRvL*, **113**, 045001
- de Jager, O. C., & Harding, A. K. 1992, *ApJ*, **396**, 161
- Ghisellini, G., Tavecchio, F., Foschini, L., et al. 2010, *MNRAS*, **402**, 497
- Giannios, D. 2013, *MNRAS*, **431**, 355
- Giannios, D., & Uzdensky, D. A. 2019, *MNRAS*, **484**, 1378
- Guo, F., Li, H., Daughton, W., & Liu, Y.-H. 2014, *PhRvL*, **113**, 155005
- Kiehlmann, S., Savolainen, T., Jorstad, S. G., et al. 2016, *A&A*, **590**, A10
- Larionov, V. M., Jorstad, S. G., Marscher, A. P., et al. 2013, *ApJ*, **768**, 40
- Loureiro, N. F., Schekochihin, A. A., & Cowley, S. C. 2007, *PhPl*, **14**, 100703
- Lyubarsky, Y. E. 2005, *MNRAS*, **358**, 113
- Lyutikov, M., Komissarov, S., Sironi, L., & Porth, O. 2018, *JPhPh*, **84**, 635840201
- Lyutikov, M., Sironi, L., Komissarov, S. S., & Porth, O. 2017, *JPhPh*, **83**, 635830602
- Lyutikov, M., & Uzdensky, D. 2003, *ApJ*, **589**, 893
- Marscher, A. P. 2014, *ApJ*, **780**, 87
- Marscher, A. P., Jorstad, S. G., D’Arcangelo, F. D., et al. 2008, *Natur*, **452**, 966
- Marscher, A. P., Jorstad, S. G., Larionov, V. M., et al. 2010, *ApJL*, **710**, L126
- Mehlhoff, J. M., Werner, G. R., Uzdensky, D. A., & Begelman, M. C. 2020, *MNRAS*, in press
- Morozova, D. A., Larionov, V. M., Troitsky, I. S., et al. 2014, *AJ*, **148**, 42
- Nalewajko, K. 2017, *Galax*, **5**, 64
- Ortuño-Macías, J., & Nalewajko, K. 2020, *MNRAS*, **497**, 1365
- Petropoulou, M., Giannios, D., & Sironi, L. 2016, *MNRAS*, **462**, 3325
- Petropoulou, M., Sironi, L., Spitkovsky, A., & Giannios, D. 2019, *ApJ*, **880**, 37
- Rowan, M. E., Sironi, L., & Narayan, R. 2017, *ApJ*, **850**, 29
- Rowan, M. E., Sironi, L., & Narayan, R. 2019, *ApJ*, **873**, 2
- Sironi, L., & Beloborodov, A. M. 2020, *ApJ*, **899**, 52
- Sironi, L., Giannios, D., & Petropoulou, M. 2016, *MNRAS*, **462**, 48
- Sironi, L., Petropoulou, M., & Giannios, D. 2015, *MNRAS*, **450**, 183
- Sironi, L., & Spitkovsky, A. 2014, *ApJL*, **783**, L21
- Sobacchi, E., & Lyubarsky, Y. E. 2020, *MNRAS*, **491**, 3900
- Spitkovsky, A. 2005, in AIP Conf. Ser. 801, Astrophysical Sources of High Energy Particles and Radiation, ed. T. Bulik, B. Rudak, & G. Madejski (Melville, NY: AIP), 345
- Uzdensky, D. A., Loureiro, N. F., & Schekochihin, A. A. 2010, *PhRvL*, **105**, 235002
- Vranic, M., Martins, J. L., Fonseca, R. A., & Silva, L. O. 2016, *CoPhC*, **204**, 141
- Werner, G. R., & Uzdensky, D. A. 2017, *ApJL*, **843**, L27
- Werner, G. R., Uzdensky, D. A., Begelman, M. C., Cerutti, B., & Nalewajko, K. 2018, *MNRAS*, **473**, 4840
- Werner, G. R., Uzdensky, D. A., Cerutti, B., Nalewajko, K., & Begelman, M. C. 2016, *ApJL*, **816**, L8
- Yuan, Y., Nalewajko, K., Zrake, J., East, W. E., & Blandford, R. D. 2016, *ApJ*, **828**, 92
- Zenitani, S., & Hoshino, M. 2001, *ApJL*, **562**, L63
- Zhang, H., Chen, X., Böttcher, M., Guo, F., & Li, H. 2015, *ApJ*, **804**, 58
- Zhang, H., Li, X., Guo, F., & Giannios, D. 2018, *ApJL*, **862**, L25